

Longitudinal Diffusion in Retinal Rod and Cone Outer Segment Cytoplasm: the Consequence of Cell Structure

David Holcman and Juan I. Korenbrot

Keck Center for Theoretical Neurobiology and Department of Physiology, School of Medicine, University of California at San Francisco, San Francisco, California

ABSTRACT Excitation signals spread along photoreceptor outer segments away from the site of photon capture because of longitudinal diffusion of cGMP, a cytoplasmic second messenger. The quantitative features of longitudinal diffusion reflect the anatomical structure of the outer segment, known to be profoundly different in rod and cone photoreceptors. To explore how structural differences affect cytoplasmic diffusion and to assess whether longitudinal diffusion may contribute to the difference in signal transduction between photoreceptor types, we investigated, both theoretically and experimentally, the longitudinal diffusion of small, hydrophilic molecules in outer segments. We developed a new theoretical analysis to explicitly compute the longitudinal diffusion constant, D_l , in terms of outer segment structure. Using time-resolved fluorescence imaging we measured D_l of Alexa488 and lucifer yellow in intact, single cones and validated the theoretical analysis. We used numerical simulations of the theoretical model to investigate cGMP diffusion in outer segments of various species. At a given time interval, cGMP spreads further in rod than in cone outer segments of the same dimensions. Across all species, the spatial spread of cGMP at the peak of the dim light photocurrent is 3–5 μm in rod outer segments, regardless of their absolute size. Similarly the cGMP spatial spread is 0.7–1 μm in cone outer segments, independently of their dimensions.

INTRODUCTION

In retinal rod photoreceptors, transduction and adaptation signals spread along the outer segment (OS) away from the site of photon capture (Hagins et al., 1970; Lamb et al., 1981; Hemila and Reuter, 1981; Matthews, 1986). Hagins et al. (1970) first proposed that cytoplasmic longitudinal diffusion of a then-undetermined second messenger could explain this spatial spread. By now, the longitudinal diffusion of the transduction messengers, cGMP (Koutalos et al., 1995a,b) and Ca^{2+} (Gray-Keller et al., 1999; Nakatani et al., 2002), as well as that of other small hydrophilic molecules (Hochstrate and Ruppel, 1980; Olson and Pugh, 1993) have been measured in rod outer segments (ROS) and have validated the original idea. For any given molecule, cytoplasmic diffusion in ROS is slower than in aqueous solution because of the mechanical hindrance imposed by the stacked disks that fill the outer segment (Olson and Pugh, 1993). In cone photoreceptors, the quantitative features of the spatial spread of excitation and adaptation are unknown and cytoplasmic longitudinal diffusion has not been previously investigated.

The terms *rod* and *cone* were first used to denote gross differences in the cytological appearance of the retinal photoreceptor outer segments. This gross difference, however, is much more prominent in nonmammalian species than in mammals. In all vertebrates, nonetheless, rods and

cones differ profoundly in the detailed cytoarchitecture of their respective OS (reviewed in Borwein, 1981). In both rods and cones, OS formation begins as an evagination of the plasma membrane at the base of the organelle (Steinberg et al., 1980; Knabe and Kuhn, 1998). In rods, the evaginations transform into collapsed disks separated from the plasma membrane over the full OS length. The intradisk volume is electrically and osmotically disconnected from the plasma membrane and from other disks (Hagins and Ruppel, 1971; Korenbrot et al., 1973). In every species studied in detail, ROS disks are ~ 150 Å thick each and are stacked with almost crystalline precision at 300 Å repeat distance (Rosenkranz, 1970; Blaurock and Wilkins, 1969). The peripheral disk edge is ~ 150 Å away from the plasma membrane. Disks are fractured by 150 Å wide incisures that start at the edge and run along the disk radius. The incisures vary in number and length among species. Their number can range from 1 in mice and humans to 18 in tiger salamander (Olson and Pugh, 1993), and they can be as long as the ROS radius (toad; Roof and Heuser, 1982) or less than one-half the radius in length (rat; Leeson, 1970; Pedler and Tilly, 1967). Disks are structurally linked by an elaborate scaffold of filaments that reach from disk to disk, from disk edge to plasma membrane and from disk edge to disk edge across the incisures (Roof and Heuser, 1982). This structural scaffolding holds disks in a stable, permanent position and, as a result, incisures in individual disks are aligned with each other, forming crevices that stretch over anywhere from 20 to 60% of the outer segment length (Clark and Branton, 1968; Korenbrot et al., 1973).

In cones, the membrane evaginations that form the OS do not close onto themselves and do not form disks separated from the plasma membrane (Nilsson, 1964, 1965; Knabe and Kuhn, 1998). The evaginations fan back and forth to create

Submitted August 26, 2003, and accepted for publication December 22, 2003.

Address reprint requests to Juan I. Korenbrot, Dept. of Physiology, School of Medicine, Box 0444, University of California at San Francisco, San Francisco, CA 94143. Tel.: 415-476-1652; Fax: 415-476-4929; E-mail: juan@itsa.ucsf.edu.

David Holcman's permanent address is Department of Mathematics and Computer Science, Weizmann Institute of Science, Rehovot 76100 Israel.

© 2004 by the Biophysical Society

0006-3495/04/04/01/17 \$2.00

folds stacked along the cone outer segment (COS) length, ordered with almost crystalline precision (Fetter and Corless, 1987). The repeat distance between successive folds is ~ 300 Å and each fold is ~ 150 Å thick. The extracellular interfold gap is ~ 150 Å thick and is continuous with the extracellular space (Cohen, 1968; Laties and Liebman, 1970). Membrane folds lack radial incisures like those in ROS. The COS membrane folds are not free-floating; they are rigidly maintained in their stable positions by an elaborate scaffold of filaments that reach from the edge of one fold to its immediate neighbors (Fetter and Corless, 1987). The plasma membrane wraps over one-half of each fold's perimeter and then fuses with the fold at two singular points, each diametrically opposite the other, referred to as *saddle points* (Fetter and Corless, 1987). Each cone membrane fold, hence, has approximately one-half its perimeter exposed to extracellular space (*open loop*) and the other half exposed to the cytoplasmic space (*closed loop*), separated by a 100 Å gap from the plasma membrane.

Elegant previous studies have shown that longitudinal cytoplasmic diffusion in ROS is well described by the standard solution of the one-dimensional diffusion equation solved for specific boundary conditions (Olson and Pugh, 1993). For several small molecules, cGMP among them, diffusion along the outer segment has been described using empiric diffusion constants, D_{long} , obtained by matching experimental data with numerical solutions (Olson and Pugh, 1993; Koutalos et al., 1995a,b). D_{long} has been inferred to reflect mechanical obstruction by rod disks as well as potential binding to cytoplasmic sites (Olson and Pugh, 1993), different than the usual theory of reaction-diffusion where D_{long} reflects only properties of motion, not binding.

Cone photoreceptors respond to light with a change in membrane current that is faster, is less sensitive to light, and which adapts over a far broader range of light intensities than do rod photoreceptors (reviewed in Pugh and Lamb, 2000). To explore how the distinct cone and rod OS structures affect cytoplasmic longitudinal diffusion and to assess whether longitudinal diffusion may contribute to the difference in signal transduction between photoreceptor types, we investigated, both theoretically and experimentally, cytoplasmic diffusion along the photoreceptor OS length. In the mathematical analysis, D_1 , the longitudinal diffusion constant in ROS and COS, is computed explicitly in terms of the cell structure. In cones, unlike rods, diffusion cannot be described by the standard linear one-dimensional diffusion equation, inasmuch as the diffusion coefficient $D_1(x)$ varies with OS length; its value can instead be derived from the known COS structure. We measured the longitudinal cytoplasmic diffusion of small, hydrophilic fluorescent molecules in single COS isolated from striped bass and examined the experimental results with the aid of the mathematical analysis. We use the mathematical analysis to predict the spread of cGMP in cones and rods, which we find to be significantly different even for OS of nearly identical dimensions.

MATERIALS AND METHODS

Materials

Striped bass (*Morone saxatilis*) were obtained from Professional Aquaculture Services (Chico, CA) and maintained in the laboratory for up to six weeks under 10:14 h dark/light cycles. The University of California, San Francisco Committee on Animal Research approved protocols for the upkeep and sacrifice of the animals. AlexaFluor 488 hydrazide, Na^+ salt, and lucifer yellow CH, lithium salt, were purchased from Molecular Probes (Eugene, OR). The aqueous diffusion constant, Da_q , at 20°C of Alexa 488 ($400 \mu\text{m}^2 \text{s}^{-1}$) were computed from the known Da_q of ATP (Bowen and Martin, 1964) and the Einstein-Stokes equation, $Da = D_b \sqrt{mw_b/mw_a}$. Enzymes for tissue dissociation were obtained from Worthington Biochemical (Lakewood, NJ). All other chemicals were from Sigma Chemicals (St. Louis, MO).

Photoreceptor isolation

Under infrared illumination and with the aid of a TV camera and monitor, retinas were isolated from dark-adapted animals, briefly treated with collagenase and hyaluronidase, and photoreceptors dissociated by mechanical trituration as described in detail elsewhere (Miller and Korenbrot, 1993). Photoreceptors were dissociated in a Ringer's solution in which glucose was replaced with 5 mM pyruvate. The standard Ringer's composition was (in mM): NaCl (136), KCl (2.4), NaHCO_3 (5), NaH_2PO_4 (1), MgCl_2 (1), CaCl_2 (1), Minimum Essential Medium amino acids and vitamins (Gibco-BRL), glucose (10), bovine serum albumin (0.1 mg/ml), and HEPES (10). The pH was 7.5 and osmotic pressure was 310 mOsm.

Cells suspended in pyruvate Ringer's solution ($\sim 150 \mu\text{l}$) were deposited onto a recording chamber held on the stage of an inverted microscope. The floor of the recording chamber was a glass coverslip covalently coated with Concanavalin A (3 mg/ml) (Picones and Korenbrot, 1992). Solitary photoreceptors were firmly attached to the coverslip and after 10 min the cell-bathing solution was exchanged with normal, glucose-containing Ringer's. The bath solution was intermittently perfused throughout the experimental session.

Membrane currents in intact, single cones

We measured membrane current under voltage-clamp using tight-seal electrodes in the whole-cell mode. Electrodes were produced from aluminosilicate glass (Corning 1724, $1.5 \times 1.0 \text{ mm od} \times \text{id}$). Using differential interference contrast (DIC) optics, a charge-coupled device camera, and monitors, and under orange ($>560 \text{ nm}$) illumination, electrodes were sealed onto the side of the inner segment. Currents were recorded with a patch-clamp amplifier (Axopatch 1D; Axon Instruments, Foster City, CA). Analog signals were low-pass-filtered below 100 Hz with an eight-pole Bessel filter (Kronh-Hite, Avon, MA) and digitized online at 200 Hz (Digidata 1200 and pClamp software, Axon Instruments, Union City, CA).

The composition of the tight-seal electrode-filling solution was (in mM): K^+ gluconate (115), K^+ aspartate (20), KCl (33), BAPTA (1), MgCl_2 (1 free), and MOPS (10). The pH was 7.25 and osmotic pressure was 305 mOsm. The solution lacked triphosphate nucleotides and, therefore, could not sustain endogenous synthesis of cGMP and phototransduction (Hestrin and Korenbrot, 1987; Rispoli et al., 1993). We included in the solution either of two fluorescent dye molecules (fluorochromes), Alexa488 (0.2 mM) or lucifer yellow (1–2.5 mM).

Image acquisition and analysis

Simultaneously with membrane current we captured fluorescent images of the single cone being recorded. We used an instrument described in detail elsewhere (Ohya et al., 2000) to observe cells with a near-ultraviolet transmitting, high numerical-aperture objective (Fluo 40 \times /1.3 NA, Nikon

Optics, Melville, NY). An epi-illumination pathway was used to bring fluorescence excitation light to the cells and fluorochrome-specific epicubes were used to spectrally separate fluorescence excitation from emission light. This epi-illumination pathway used a DC-operated Xe light source and included an electromechanical shutter and a pinhole aperture. The aperture restricted fluorescence excitation to a 45- μm -diameter circle centered on the cell under investigation and the shutter was controlled to limit epifluorescent illumination only to those times images were being acquired. Excitation light intensity at the plane occupied by cells on the microscope stage was relatively dim (460–500 nm, 4×10^{-3} Cd m $^{-2}$) to minimize dye photobleaching. We acquired high-resolution images with a cooled, high-resolution interline charge-coupled device camera (MicroMAX, Princeton Instruments, Trenton, NJ; 5 MHz, 1300(H) \times 1030(V) pixels, 6.7 μm \times 6.7 μm pixels center to center) operated with appropriate controller and image acquisition boards and software (WinView3.2, Roper Scientific, Trenton, NJ). The optical system could be readily switched to operate either under DIC illumination (for electrophysiological recordings) or epifluorescence.

In general, a cell was selected for investigation and its image first captured under DIC optics. Under video observation a tight-seal electrode was applied onto the surface of the inner segment and a gigaseal formed. Epifluorescent illumination was then engaged and successive single images captured, each integrated over 0.5–1.5 s, depending on the fluorochrome and its concentration. Integrated single images were acquired every 3 or 5 s, again depending on the fluorochrome and its concentration.

We only analyzed fluorescent images of healthy cells in which the electrode seal remained intact. In successful experiments, current and images were simultaneously collected for 3–15 min. Using commercially available image analysis software (C. Imaging, Compix, Cranberry Township, PA), each cell's DIC image was first measured to determine cellular dimensions and to design a fluorescence-sampling grid. The grid consisted (depending on cell dimensions) of between 49 and 63 rectangular elements; each element was 0.25–0.31 μm along the OS length and their transverse dimension was equal to the diameter of the outer segment's base. Each rectangular element was oriented with its transverse (long) dimension perpendicular to the outer segment's longitudinal axis and placed, without a gap, adjacent to its neighboring element. The full set of individual elements covered the entire COS length. Each cell was analyzed with a unique sampling grid designed following the rules stated above, but every single image of a given cell was analyzed with the same grid. Fluorescent intensity was measured at 10-bit resolution as the mean gray level of each element in the sampling grid. Image acquisition was begun before whole-cell mode was attained, thus we always measured the background gray level in the unloaded outer segment. This background fluorescence is shown as a continuous line in the experimental data presented in this report.

A THEORY OF LONGITUDINAL DIFFUSION

General description

In this section we present a mathematical analysis of cytoplasmic longitudinal diffusion in COS and ROS. In this analysis, one-dimensional diffusion equations are derived from first principles and diffusion coefficients are explicitly computed in terms of ROS and COS cytoarchitecture. The method is sufficiently general to be applicable to any cell of known geometry. The principle of the analysis is to reduce the three-dimensional diffusion equation into a one-dimensional equation by averaging over the other two dimensions through detailed consideration of the geometrical organization of the cell. For ROS and COS, the longitudinal diffusion equation is defined as the geometrical reduction of the diffusion equation when the averaging directions are orthog-

onal to the long axis of the OS. We refer to this process as a geometrical reduction of the three-dimensional diffusion equation.

The derived diffusion equations compute the change in the average concentration along the OS. By definition, the concentration is the number of free particles per volume confined to move in the OS cytoplasm and restricted by disks (in rods) or foldings (in cones) that are impenetrable barriers. The following analysis reveals that because of translational invariance, the longitudinal diffusion equation in rods is the standard diffusion equation with constant longitudinal diffusion coefficient. In COS, in contrast, the diffusion coefficient is not a constant value, but changes with longitudinal position.

Aqueous diffusion in the outer segment cytoplasm, model, and simplifications

Brownian particles in the OS are driven by thermal noise and their trajectory in the cytoplasm is well described by the overdamped approximation (Smoluchowski limit) of the Langevin equation. Thus, for a molecule located at position $x(t)$, in the limit of large viscosity coefficient, the velocity satisfies the stochastic equation

$$\gamma \dot{X} + F(x) = \sqrt{2\gamma\epsilon} \dot{w}, \quad (1)$$

where $F(x)$ are forces applied onto the particle, γ is the viscosity coefficient, $\epsilon = kT/m$ is the thermal noise, and \dot{w} is the white noise produced by thermal collisions (Schuss, 1980).

To study Eq. 1, we make three assumptions:

1. Particles do not bind.
2. In the timescale of seconds, short-range electrostatic interactions that arise from the charged disk membrane surfaces (McLaughlin and Brown, 1981) and/or charged particles in solution average and cancel out. As a consequence all electrostatic terms are neglected and the force term $F(x)$ in Eq. 1 is set to 0.
3. Particles do not permeate across OS membranes.

From the general theory of diffusion, it is well known that the probability density function (pdf) of one molecule associated with Eq. 1 satisfies the standard three-dimensional diffusion equation in the cytoplasm. Under the assumption of independent molecules, the concentration is simply the product of the pdf by the number of molecules and satisfies the following diffusion equation within the OS,

$$\frac{\partial c}{\partial t} = D\Delta c, \quad (2)$$

$$c(x, 0) = c_0(x), \quad (3)$$

where $c_0(x)$ is some initial concentration, and D is the diffusion constant given by Schuss (1980), as

$$D = \frac{kT}{m\gamma}, \quad (4)$$

where m is the mass of the molecule, γ the viscosity coefficient, T the absolute temperature, and k the Boltzmann constant.

Longitudinal diffusion in rod outer segments

Definition of a rod compartment

ROS consists of repeating spatial compartments, U_k (Fig. 1). Each compartment comprises the distance from one disk surface to the comparable surface in the next disk. The repeat distance is l , and it consists of two equal parts: the cytoplasmic space separating two adjacent disks (interdisk space, dimension = $l/2$) and the disk itself (dimension = $l/2$).

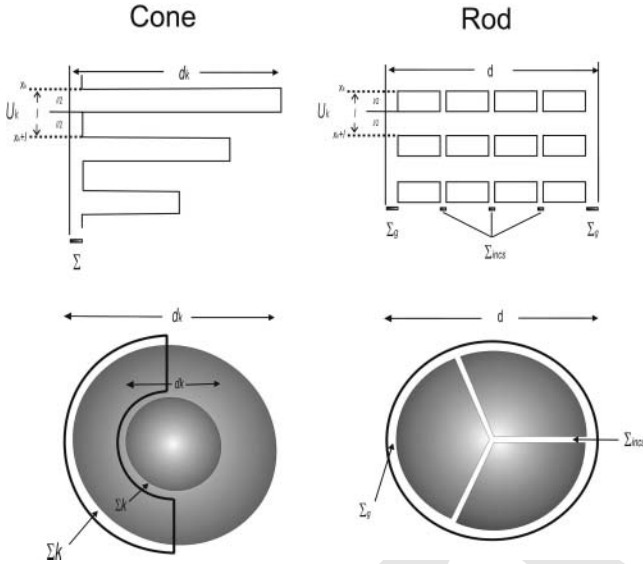


FIGURE 1 Schematic representation of cone and rod outer segment structure. In cones, the outer segment membrane fans back and forth to create folds. In our analysis we define a single compartment (U_k) as the distance from the intracellular surface of one membrane fold to the intracellular surface of the next. The repeat distance is l and it consists of two segments: the membrane fold (dimension = $l/2$) and the distance separating one fold from the next (dimension = $l/2$). The connection between adjacent folds is represented by a cylinder of length = $l/2$ and diameter = r . The diameter of a fold at position x_k is denoted by d_k and it increases linearly with outer segment length from the base to the tip. There also exists a surrounding plasma membrane that is separated from the membrane folds. Over the full COS length, the plasma membrane wraps over approximately one-half of the outer segment's perimeter and fuses with the edge of each membrane fold at two singular saddle points. Σ is the surface area of the hemitoroidal gap between the closed loop of the membrane fold and the plasma membrane. In rods, collapsed membrane vesicles form a stack of disks electrically and osmotically separated from a surrounding plasma membrane. The unit compartment U_k has a diameter d , and it encompasses the longitudinal distance from one disk surface to the same surface in the next disk. The repeat distance is l , and it consists of two segments: the cytoplasmic space separating two adjacent disks (interdisk space, dimension = $l/2$) and the disk itself (dimension = $l/2$). Σ_g is the area of the gap that separates each disk's perimeter from the surrounding plasma membrane. Disks are fractured by 150 Å wide radial incisures and the surface area of this incisure gap is Σ_i .

Diffusion between adjacent interdisk spaces occurs either through disk incisures or the perimetric gap that separates disk edges from the plasma membrane. The compartment's radius is constant and denoted by r . We adopt the following notation: N_k is the number of free Brownian particles in the U_k compartment of volume V_k .

Derivation of the diffusion equation

The objective of the following derivation is to compute the ROS longitudinal diffusion constant, D_l , in terms of the cell's structure. Variation in the number of particles in unit U_k equals the difference of flux into compartments $k-1$ and $k+1$; that is,

$$\frac{dN_k(t)}{dt} = \int_{U_k} \frac{\partial c(x,t)}{\partial t} dV = -D[J_k - J_{k+1}]. \quad (5)$$

By definition, J_{k+1} is the flux between unit U_k and U_{k+1} through Σ_{k+1} , the open surface that joins them, as

$$J_{k+1} = \int_{\Sigma_{k+1}} -D \frac{\partial c(x,t)}{\partial n(x)}, \quad (6)$$

where $n(x)$ is the normal derivative pointing outside U_k and $\partial U_k = \Sigma_{k+1} \cup \Sigma_k$.

In the timescale of seconds, concentration is assumed to be uniform within each U_k compartment. This assumption is valid because diffusion along the longitudinal axis is much slower than along the transverse axis (Olson and Pugh, 1993). This fact follows from:

1. Diffusion within a compartment (transverse diffusion) is given by the standard two-dimensional diffusion process and is limited only by aqueous diffusion and not by anatomical constraints (Schuss, 1980).
2. The ratio of the absorbing boundary surface divided by the reflective boundary surface of a given compartment is small.

Combining Eqs. 5 and 6 yields

$$\frac{1}{V_k} \frac{dN_k(t)}{dt} = \frac{D}{V_k} (n\Sigma_{\text{incs}} + \Sigma_g) \left(\frac{\partial c(x_{k+1}, t)}{\partial x} - \frac{\partial c(x_k, t)}{\partial x} \right), \quad (7)$$

where Σ_{incs} is the surface area of a single disk incisure, n is the number of incisures, and Σ_g is the surface of the perimeter gap between the disk's edge and plasma membrane; and $\Sigma_g = 2\pi r g_w$, where r is the ROS radius and g_w is the size of the perimeter gap.

The concentration at points $x_{k+1} = x_k + l$ and x_k is evaluated by a Taylor expansion. At the first order, inasmuch as $c(x_k, t) = N_k(t)/V_k$, then

$$\frac{\partial c(x_k, t)}{\partial t} = \frac{1}{V_k} \frac{dN_k(t)}{dt} = \frac{D}{V_k} (n\Sigma_s + \Sigma_l) l \frac{\partial^2 c(x_k, t)}{\partial x^2}. \quad (8)$$

The translation invariance of the rod outer-segment geometry implies that the volume V_k of the compartment U_k is constant with respect to k and equals the free intracellular volume (free volume of the unit plus the free volume of the incisures), as

$$\begin{aligned} V_k &= \pi r_k^2 l/2 + nV_{\text{incs}} + V_g \\ &= \pi r^2 l/2 + (n\Sigma_s + 2\pi r g_w)l/2, \end{aligned} \quad (9)$$

where V_{incs} is the volume of the incisure and V_g is the volume of the perimeter gap. Finally, Eq. 8 can be reduced to the form of the standard one-dimensional diffusion equation,

$$\frac{\partial c(x,t)}{\partial t} = D_1 \frac{\partial^2 c(x,t)}{\partial x^2}, \quad x \text{ in } [0, L], \quad (10)$$

where the longitudinal diffusion constant is defined to be

$$D_1 = \frac{D(n\Sigma_{\text{incs}} + \Sigma_g)l}{\pi r^2 l/2 + (n\Sigma_{\text{incs}} + \Sigma_g)l/2} = 2D \frac{1}{\frac{\pi r^2}{n\Sigma_{\text{incs}} + \Sigma_g} + 1}. \quad (11)$$

Longitudinal diffusion in cone outer segments

Definition of cone compartment

COS consists of repeating U_k compartments, each comprising the distance from the intracellular surface of one membrane fold to the intracellular surface of the next one (Fig. 1). The repeat distance is l and it consists of two segments: the membrane fold (dimension = $l/2$) and the distance separating one fold from the next (dimension = $l/2$). In reality, the surface connecting adjacent folds is the hemitorus between the fold's closed loop and the plasma membrane (Fig. 1) (Fetter and Corless, 1987). We assume that, on average, the geometry of this surface does not change with COS length and is well approximated by a cylinder of length = $l/2$ and diameter δ . That is, δ is the diameter of a circle of area equal to the area of the toroidal surface. We refer to δ as the equivalent diameter. The diameter of a membrane fold at position x_k is denoted by d_k . d_k increases linearly with the longitudinal coordinate as given by $d_{k+1} = d_k + d_0$, where d_0 is the unitary increment in diameter between immediately adjacent folds.

Derivation of the diffusion equation

Derivation of the longitudinal diffusion equation in COS proceeds through the same steps as the derivation for ROS, but the end result differs because the spatial compartments, U_k , change with COS length. As in ROS, the time variation in the particle number in the U_k compartment is given by Eq. 5 and the flux through the Σ_{k+1} surface is given by

Eq. 6. From these equations, the variation in time of the concentration in a COS compartment is given by

$$\frac{1}{V_k} \frac{dN_k(t)}{dt} = \frac{1}{V_k} \left(D\Sigma_{k+1} \frac{\partial c(x_{k+1}, t)}{\partial n(x)} - D\Sigma_k \frac{\partial c(x_k, t)}{\partial n(x)} \right). \quad (12)$$

Inasmuch as $\Sigma_{k+1} = \Sigma_k$, using a Taylor expansion of the concentration $c(x,t)$, we have

$$\frac{\partial c(x_k, t)}{\partial t} = \frac{1}{V_k} \frac{dN_k(t)}{dt} = \frac{D\Sigma_{k+1}l}{V_k} \frac{\partial^2 c(x_k, t)}{\partial x_k^2}. \quad (13)$$

The area of the surface Σ_{k+1} is given by $\Sigma_{k+1} = \pi(\delta/2)^2$ and its volume is

$$V_k = \pi(\delta/2)^2 l/2 + \pi(d_k/2)^2 l/2. \quad (14)$$

We define d_{min} as the smallest COS diameter (at the tip), d_{max} as the largest diameter (at the base), and L as the COS length. Furthermore,

$$\alpha = \frac{d_{\text{max}} - d_{\text{min}}}{L}. \quad (15)$$

Because of the cone geometry, at position x_k the cone diameter is $d_k = \alpha x_k + d_{\text{min}}$, and the longitudinal diffusion equation can now be expressed as

$$\begin{aligned} \frac{\partial c(x_k, t)}{\partial t} &= \frac{D\pi(\delta/2)^2 l}{\pi(\delta/2)^2 l/2 + l/8\pi(\alpha x_k + d_{\text{min}})^2} \\ &\times \frac{\partial^2 c(x_k, t)}{\partial x_k^2}; \end{aligned} \quad (16)$$

but for $x \in [0, L]$, the equation simplifies to

$$\frac{\partial c(x, t)}{\partial t} = \frac{2D\delta^2}{\delta^2 + (\alpha x + d_{\text{min}})^2} \frac{\partial^2 c(x, t)}{\partial x^2}. \quad (17)$$

The longitudinal diffusion coefficient (which is now, in one dimension, a function of x) is explicitly given by

$$D(x) = \frac{2D\delta^2}{\delta^2 + (\alpha x + d_{\text{min}})^2}. \quad (18)$$

Determination of the anatomical diameter function $\delta_a(x)$ from the COS structure

Given the COS structure, Eq. 17 can be modified to include a spatial dependency on the δ -variable. Recall that the COS geometry is characterized by the following global parameters. L is the length, r_{base} is the radius at the base, r_{tip} is the

radius at the tip, and $\alpha' = (r_{\text{base}} - r_{\text{tip}})/L$. The hemitoroidal surface connecting adjacent folds at the longitudinal position x is $\Sigma_g(x)$. If $r_m(x)$ is the radius up to the plasma membrane and $r_f(x)$ is the radius of the membrane fold at position x , then the area of $\Sigma_g(x)$ is (see Fig. 1)

$$\Sigma_g(x) = \frac{\pi}{2} (r_m(x)^2 - r_f(x)^2), \quad (19)$$

for $r_{\text{tip}} \leq r_f(x) \leq r_{\text{base}}$,

$$r_f(x) = r_{\text{tip}} + \alpha'x, \quad (20)$$

$$r_m(x) = r_f(x) + \Delta r. \quad (21)$$

The gap Δr between the closed loop of a fold and the plasma membrane is ~ 100 Å; that is, $\Delta r = r_m - r_f = 0.01$ μm is small compared to r_m . For that reason, we can approximate $\Sigma_g(x)$ as

$$\Sigma_g(x) = \pi \Delta r r_f(x) = \pi \Delta r \left(r_{\text{tip}} + \left(\frac{r_{\text{base}} - r_{\text{tip}}}{L} \right) x \right). \quad (22)$$

Let us define the anatomical diameter function $\delta_a(x)$ as the diameter of a circle whose area is identical to that of $\Sigma_g(x)$. Thus,

$$\Sigma_g(x) = \pi (\delta_a(x)/2)^2 \quad (23)$$

and

$$\delta_a(x) = 2\sqrt{\Delta r (r_{\text{tip}} + \alpha'x)}. \quad (24)$$

We can now define the average surface, $\bar{\Sigma}_g$, along the COS by

$$\begin{aligned} \bar{\Sigma}_g &= \frac{1}{L} \int_0^L \Sigma_g(x) dx = \frac{1}{L} \int_0^L \pi \Delta r r_f(x) dx \\ &= \pi \Delta r \frac{r_{\text{base}} + r_{\text{tip}}}{2}. \end{aligned} \quad (25)$$

The average diameter, $\bar{\delta}_a$, is

$$\bar{\delta}_a = 2\sqrt{\frac{\bar{\Sigma}_g}{\pi}} = 2\sqrt{\Delta r \frac{r_{\text{tip}} + r_{\text{base}}}{2}}. \quad (26)$$

Cone diffusion longitudinal equation

Using the result of the previous section, the function $\delta(x)$ can be incorporated into the cone diffusion equation and Eq. 16 becomes

$$\frac{\partial c(x, t)}{\partial t} = \frac{2D\delta(x)^2}{\delta(x)^2 + (x\alpha + d_{\text{min}})^2} \frac{\partial^2 c(x, t)}{\partial x^2}, \quad (27)$$

with

$$\delta(x) = 2\sqrt{\Delta r (r_{\text{tip}} + \alpha'x)}. \quad (28)$$

The diffusion coefficient is now given by

$$\tilde{D}(x) = \frac{4D\Delta r}{(d_{\text{tip}} + \alpha x) + 4\Delta r}, \quad (29)$$

and the cone diffusion equation becomes

$$\frac{\partial c(x, t)}{\partial t} = \tilde{D}(x) \frac{\partial^2 c(x, t)}{\partial x^2}. \quad (30)$$

Spread space constant in a rod outer segment, λ_{rod}

To evaluate the longitudinal spread of any molecule, space constants for COS and ROS are defined using the equations derived above. The result of this section is used to compare the spread of excitation in rods versus cones.

Since the diffusion equation in ROS is linear, the second moment of the probability density function of the diffusion process p , conditioned by the initial location of the source at position x_0 , defines, at each moment in time, a spread length constant $\lambda_{\text{rod}}(t)$. In an ROS of length L , the second moment is defined by

$$\lambda_{\text{rod}}(t) = \frac{1}{2} \int_0^L x^2 p(x, t|x_0) dx. \quad (31)$$

The spread space constant λ_{rod} for rods is defined as the value of $\lambda_{\text{rod}}(t)$ for $t = t_p$, where t_p is the time to peak of a photoresponse. The value t_p is a fundamental characteristic of the response time of a rod to a single photon,

$$\lambda_{\text{rod}} = \frac{1}{2} \int_0^L x^2 p(x, t_p|x_0) dx, \quad (32)$$

when L is large, and λ_{rod} is independent of the initial position x_0 and is well approximated by the standard deviation of a free diffusion process. Thus,

$$\lambda_{\text{rod}} = \sqrt{D_1 t_p}. \quad (33)$$

Spread space function in a cone outer segment, $\lambda_{\text{cone}}(x)$

As described above, longitudinal diffusion in COS differs from that in ROS in two major respects:

1. The diffusion equation in COS is not symmetric with respect to its initial position and this lack of symmetry implies that the first moment or the mean displacement is not 0.

2. An exact solution of the cone longitudinal diffusion equation is not known; therefore, it cannot be used to estimate the moments of the pdf. In the Appendix, however, we present an exact solution valid under restricted conditions.

To compare diffusion in ROS and COS, nonetheless, an approximation can be used to define a spread space function in cones $\lambda_{\text{cone}}(x)$ at the time of the photocurrent peak, comparable to that defined above for rods. We define a spread function, rather than a spread constant because, recall, diffusion in COS varies with their length. To compute explicitly the spread function $\lambda_{\text{cone}}(x_0)$, we make the approximation that $D_1(x) = D_1(x_0)$ —that is, $D_1(x)$ is constant and equal to its value at the initial position x_0 . This approximation is justified because the time to peak t_p in cones is much briefer than in rods and, hence, the spatial spread in COS is much less extensive than in rods, as we demonstrate below (under Discussion). Under the stated approximations, the first moment of the approximated pdf vanishes and the spread function $\lambda_{\text{cone}}(x_0)$ is defined as in rods,

$$\lambda_{\text{cone}}(x_0) = \frac{1}{2} \int_0^L x^2 p(x, t_p | x_0) dx, \quad (34)$$

where p is the solution of the cone longitudinal equation. The explicit expression for $\lambda_{\text{cone}}(x_0)$ is given by

$$\lambda_{\text{cone}}(x_0) = \sqrt{D_1(x_0)t_p}. \quad (35)$$

Note that in Eq. 35, the dependency on x_0 cannot be ignored because D_1 varies in value along the COS. The spread function $\lambda_{\text{cone}}(x_0)$ keeps track of the location of the initially depleted compartment. This is a significant difference compared to the single spread constant obtained for rods. Equation 35 ignores the asymmetrical profile of the diffusion in COS.

Matching computational simulations and experimental data in bass single COS

Inasmuch as Eq. 17 describes the evolution of the longitudinal concentration c in a COS, to analyze the experimental data the boundary conditions have to be specified. At the COS tip, the origin of the coordinate is ($x = 0$). Since the particles cannot escape (no leak) and are reflected, the flux to vanish is imposed. That is,

$$\left. \frac{\partial c(x, t)}{\partial x} \right|_{x=0} = 0. \quad (36)$$

At the base of the COS, we impose a Dirichlet boundary condition, to match the concentration imposed by the experiment. The concentration equals the time-dependent

concentration $C_L(t)$ of the diffusing dyes at the COS base (where $x = L$),

$$c(x, t)|_{x=L} = C_L(t). \quad (37)$$

Since fluorescence intensity is proportional to particle number, not their concentration, the concentration $c(x, t)$ is converted into particle number $N(x, t)$ located in the compartment $U(x)$ by simply writing

$$N(t, x) = c(x, t)\phi(x), \quad (38)$$

where $\phi(x) = d(\text{Vol}U(x))/dx$ is the infinitesimal volume of a compartment, located at position x . The total number of particles in the OS at time t is

$$N(t) = \int_0^L c(x, t)\phi(x)dx. \quad (39)$$

Spatial specifications

The function $\phi(x)$ reflects the change of the geometry of the COS as a function of x . For the geometry of a generic cone of base radius r_{base} , tip radius r_{tip} , and length L ,

$$\phi(x) = \pi(\alpha'x + r_{\text{tip}})^2 \quad \text{for } x \in [0, L], \quad (40)$$

where

$$\alpha' = \frac{r_{\text{base}} - r_{\text{tip}}}{L_h}. \quad (41)$$

Specific features of COS in striped bass single cones

In single bass cones, the OS tapers smoothly from their base to a point L_h approximately midway up the length. At that point, which we name *the taper transition point*, there occurs a small change in the slope of the COS walls which then proceed smoothly to a truncated tip (see Figs. 2 and 3). Thus, for bass cones, the density function is

$$\phi(x) = \pi(\alpha_1x + r_{\text{tip}})^2 \quad \text{for } x \in [0, L_h] \quad (42)$$

$$= \pi(\alpha_2x + r_h)^2 \quad \text{for } x \in [L_h, L], \quad (43)$$

where r_h is the radius at location L_h and

$$\alpha_1 = \frac{r_h - r_{\text{min}}}{L_h}, \quad \alpha_2 = \frac{r_{\text{max}} - r_h}{L - L_h}. \quad (44)$$

To match the mathematical model with the experimental data in cones, we used Eq. 17 where δ , the equivalent diameter, is unknown, but all other parameters are known for each cell investigated: d_{min} , r_{tip} , tip diameter and radius; d_{max} , r_{base} , base diameter and radius; and L , length and L_h , taper transition point. To determine the value of δ , we fit experimental data with the results of simulations computed with varying values of δ . The cone geometry imposes that

the steady-state solution (number of particles) is proportional to the surface of the membrane fold. Thus,

$$r_h = r_{\max} \sqrt{\frac{N_{r_h}}{N_{\max}}}, \quad (45)$$

where N_{r_h} is the number of particles at location r_h .

EXPERIMENTAL RESULTS

We measured cytoplasmic longitudinal diffusion rates of Alexa488 ($mw = 570$, $Daq = 400 \mu\text{m}^2/\text{s}$) and lucifer yellow ($mw = 457$, $Daq = 430 \mu\text{m}^2/\text{s}$) in the outer segment of intact single cones isolated from striped bass. In voltage-clamped cones, we measured membrane current at -40-mV holding voltage and simultaneously acquired the cell's fluorescent image. Images and currents measured with a tight-seal electrode filled with 0.2 mM Alexa488 are shown in Fig. 2. These data are typical of every cell studied. After membrane rupture the current was initially inward, and then smoothly changed over the next minute or so until it reached a stationary outward value. For 12 cones, the mean steady-state outward current was $17.7 \pm 7.2 \text{ pA}$. Throughout the current measurement we presented, once every 3 s, a 0.5-s light flashed to generate the fluorescent images. At first, the flashes caused a cessation of the inward current; this photocurrent, however, was progressively smaller in amplitude and irreversibly disappeared $\sim 1 \text{ min}$ after achieving whole-cell mode (WCM). Both changes in holding current and loss of photoresponse arise from the exchange/replacement of the cell's cytoplasmic content by the electrode-filling solution. Because this solution lacked triphosphate

nucleotides the photoreceptor could not synthesize cGMP and, hence, cGMP-gated ion channels in the outer segments closed as the nucleotide was lost by diffusion. In the steady state, phototransduction ceased and net membrane current revealed outward flux through voltage-gated K^+ channels located in the cone inner segment membrane (Barnes and Hille, 1989; Maricq and Korenbrot, 1990). This electrical behavior is characteristic of healthy, uncompromised cones.

In Fig. 2, an arrowed line links each fluorescent image to the test flash that generated it. At the far left is a DIC image of the same cell captured immediately before the test flash sequence began. Preceding rupture of the membrane seal, fluorescence was only detected within the electrode. Upon attaining whole-cell mode the inner segment cytoplasm immediately began to fill with the dye. After a short delay, Alexa began to flow into the outer segment, across the connecting cilium. At the same time, the dye began to fill the accessory outer segment—an appendage characteristic of fish cones that connects directly to the inner segment (Januschka et al., 1987). The change in fluorescence reveals the flow of Alexa488 from the pipette lumen into the cell's cytoplasm driven by its concentration gradient and limited by the fluorophore's diffusion rate within the cell.

Longitudinal diffusion of Alexa488 in single cone outer segments

To characterize Alexa488 diffusional flow along the COS length, we measured fluorescence intensity using sampling grids consisting of multiple rectangular elements, each as wide as the COS base, positioned side by side along the OS

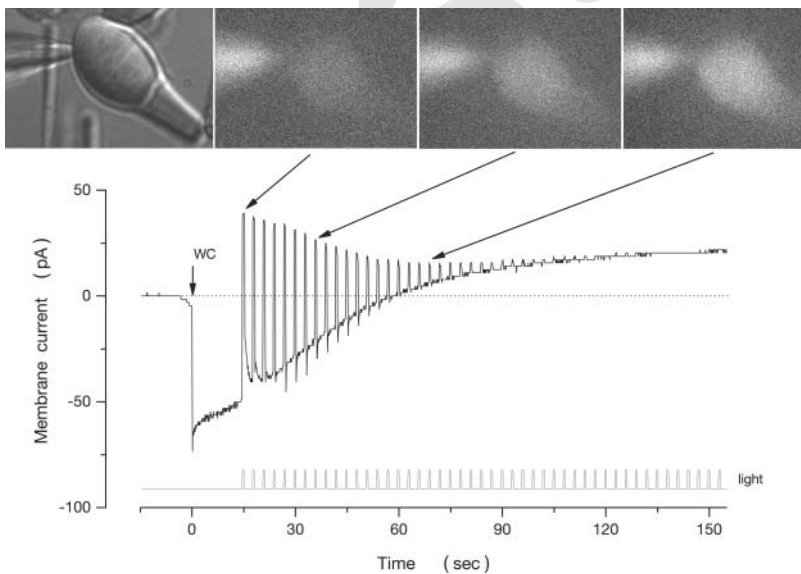


FIGURE 2 Filling of a single bass cone by diffusion of Alexa488 from a tight-seal electrode. The far-left image was captured under DIC illumination and shows the cell with the electrode sealed onto its inner segment. Fluorescent images shown were selected from a collection obtained by repeated 0.5-s epi-illumination flashes (presented once every 3 s, at the marks labeled as *light*). We designate as 0 the time whole-cell mode (WCM) is first achieved. The arrowed line links fluorescent images with the illumination flashes used to generate that image. Cytoplasmic fluorescence intensity increased progressively, first in the inner segment and then in the outer segment. Also shown is the membrane current measured as the images were being captured. At -40 mV holding voltage, the current was inward immediately upon achieving WCM, but slowly changed to a stationary outward value. Initially, the photoreceptor responded to the test light flashes with the expected cessation of inward current. The photocurrent, however, progressively diminished in amplitude in parallel with the change in holding current and ceased when the holding current reached its steady-state, outward value. The changes in electrical behavior and fluorescence reflect the exchange of contents between the cell and the electrode lumen: the cell is filled with Alexa488 and is depleted of its endogenous cGMP.

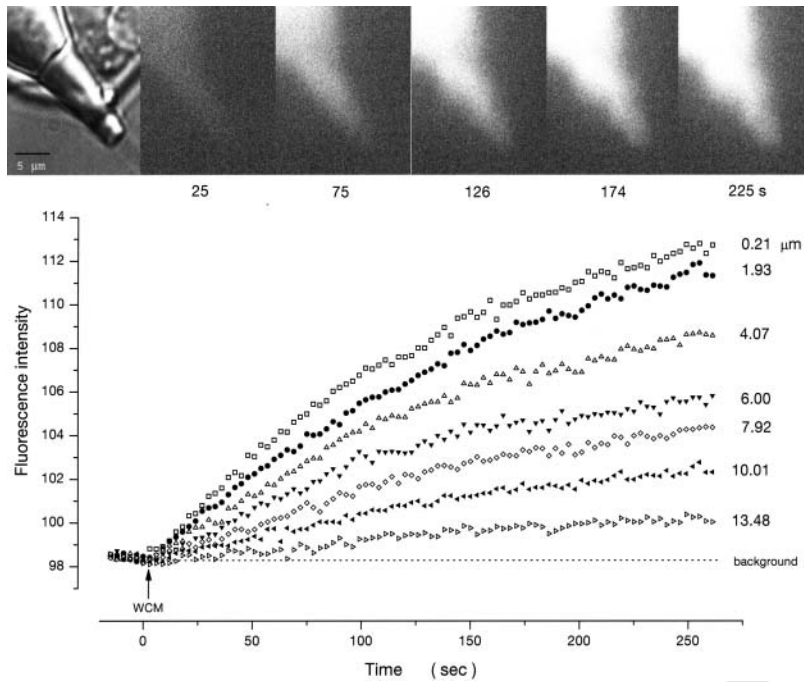


FIGURE 3 Time course of single COS filling with Alexa488. The far left is a DIC image of the COS of the intact single cone analyzed in this figure. COS dimensions were length = $13.48 \mu\text{m}$, base diameter = $6.68 \mu\text{m}$, and tip diameter = $2.78 \mu\text{m}$. One-hundred fluorescent images were acquired at 3-s intervals, each generated by a 0.5-s epi-illumination flash. Shown are selected images each acquired at various times after achieving WCM, as labeled. Fluorescence intensity was measured using a sampling grid consisting of 63 elements placed adjacent to each other over the entire COS length (see Materials and Methods). Each element was $6.7 \mu\text{m}$ in the transverse axis by $0.21 \mu\text{m}$ in the longitudinal one, and laid perpendicular to the COS longitudinal axis. The time course of change in fluorescence intensity at selected positions along the COS length is shown in the graph. Before achieving WCM (designated as $t = 0$) COS fluorescence intensity was the same as background; after WCM, fluorescence intensity increased steadily, first at the COS base and eventually at its tip, revealing the longitudinal flux of Alexa488.

length (details under Materials and Methods). The dimension of the individual elements in the sampling grid along the COS length defined the spatial resolution in our measurements (mean = $0.30 \pm 0.05 \mu\text{m}$, $n = 13$). Fig. 3 illustrates the rate of change in the fluorescence intensity measured at fixed positions along the length of the COS shown, with its base defined as the origin. Results shown are typical of every cell we analyzed ($n = 6$). The COS fluorescence intensity initially did not differ from that of the background (which arises from the optical crosstalk between fluorescence excitation and emission filters in the microscope). After attaining WCM, however, specific COS fluorescence intensity increased steadily over the course of tens of seconds. Since dye flows into the outer segment through the cilium connecting inner and outer segments, it was not surprising to observe that fluorescence increased at the base of the COS ahead of the rise at its tip.

We used the theoretical analysis detailed above to analyze the COS spatial fluorescent pattern in the course of Alexa488 filling. The mathematical analysis details the spatial distribution of Alexa488 concentration along the COS length at any time between the start of diffusion and the steady-state filling (saturation) of the cell. In Fig. 4 we present the spatial pattern of fluorescence intensity measured in three different COS loaded with 0.2 mM Alexa488 (*symbols*). For analytical reasons, in these graphs we designated the COS tip as the origin of the spatial variable. For each cell, we show the spatial pattern at various times after achieving WCM, a moment we define as time 0 .

Through computation we generated solutions to the geometrically reduced diffusion equation for a COS. The analytical model defines diffusion to occur from fold to fold

across an equivalent circular surface of diameter δ . We matched by eye the experimental and computed fluorescence spatial pattern by adjusting the value of δ . The values of all other independent variables are known from direct anatomical measurements of the COS. In Fig. 4 we present as continuous curves the computed fluorescence spatial pattern expected at various times after diffusion into the COS starts (as labeled). For each cell analyzed (Fig. 4, A–C), we selected a single value of δ that yielded the best match between computed and observed patterns of fluorescence for all times. We obtained reasonably good matches between data and simulations, and the results shown in Fig. 4 depict the range of the quality of the matches. Our results indicate that the mathematical analysis describes well the diffusion of Alexa488 in the COS, which arises from Brownian motion restricted only by the cell cytoarchitecture.

In Table 1 we present the collected results of the analysis of Alexa488 diffusion in six different COS. A salient feature inferred from our analysis and data is that the diffusion coefficient in COS is not constant, but changes with longitudinal position as given by Eq. 17. We illustrate this feature in Table 1 by presenting the computed values of D_1 at the base and tip of the COS. For all cells, the mean ratio of the diffusion constant at the base over that at the tip was 6.5 ± 0.7 .

Longitudinal diffusion of lucifer yellow single cone outer segments

Analysis of cytoplasmic diffusion can be confounded if the sampling probe binds to intracellular sites (Olson and Pugh, 1993; Koutalos et al., 1995a,b). As an experimental control

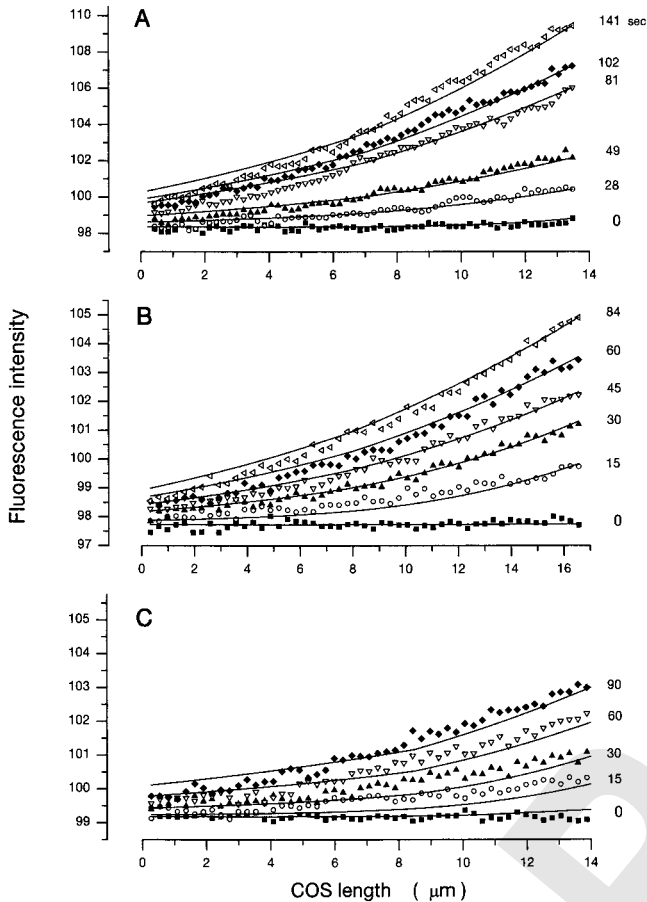


FIGURE 4 Spatial pattern of fluorescence intensity at various times after the start of Alexa488 diffusion into single bass COS. Data measured in three different cells are shown. (A) The COS dimensions were length = 13.48 μm , base diameter = 6.68 μm , and tip diameter = 2.78 μm . Fluorescence was sampled with a grid consisting of 63 elements, each 6.7 μm in the transverse axis by 0.21 μm in the longitudinal one. (B) The COS dimensions were length = 13.52 μm , base diameter = 6.29 μm , and tip diameter = 2.59 μm . Fluorescence was sampled with a grid consisting of 51 elements, each 6.9 μm in the transverse axis by 0.32 μm in the longitudinal one. (C) The COS dimensions were length = 16.57 μm , base diameter = 6.87 μm , and tip diameter = 3.11 μm . Fluorescence was sampled with a grid consisting of 61 elements, each 6.9 μm in the transverse axis by 0.27 μm in the longitudinal one. The continuous curves are solutions of the geometrical reduction of the diffusion equation we have derived (see A Theory of Longitudinal Diffusion). The lines describe Alexa concentration as a function of cell longitudinal position, each at a fixed time (as labeled), where $t = 0$ is the moment WCM is achieved and diffusion begins. Values of the adjustable parameters that generated the curves: (A) $\delta = 0.316 \mu\text{m}$ (the equivalent diameter of the circular surface that joins adjacent COS folds) and $L_h = 7.0 \mu\text{m}$ (the location of the taper transition point); (B) $\delta = 0.346 \mu\text{m}$ and $L_h = 6.49 \mu\text{m}$; and (C) $\delta = 0.316 \mu\text{m}$ and $L_h = 8.62 \mu\text{m}$.

for the adequacy of Alexa488 as a nonbinding probe we characterized the diffusion in COS of a second fluorescent molecule, lucifer yellow (LY). LY ($\epsilon = 11,000$) fluoresces less intensely than Alexa488 ($\epsilon = 71,000$). Therefore, to obtain LY fluorescence intensity data with signal/noise characteristics comparable to the Alexa488 data, we loaded cells with 1–2.5 mM dye and integrated fluorescence image

acquisition for 1.4–2 s. If binding does not occur, diffusion of LY and Alexa488 should be determined by cytoarchitecture alone.

We measured voltage-clamped current and fluorescence images of single cones while loading their cytoplasm with LY. Healthy cones exhibited electrical behavior similar to that illustrated in Fig. 1 and diffusion was only analyzed in these cells. For LY-loaded photoreceptors mean steady-state outward current was $10.7 \pm 6.6 \text{ pA}$ ($n = 13$). We repeatedly acquired fluorescence images at 5-s intervals and, afterwards, measured their fluorescence intensity with spatial grids similar to those used with Alexa488 with nearly identical spatial resolution (mean = $0.30 \pm 0.06 \mu\text{m}$, $n = 9$). In Fig. 5 we illustrate the rate of change in fluorescence intensity at fixed positions along a COS loaded with LY. After attaining WCM, fluorescence intensity increased steadily over the course of tens of seconds, starting at the COS base. This temporal pattern, observed in every cell analyzed ($n = 6$), demonstrates the diffusional flow of LY from the inner to the outer segment through the connecting cilium. The COS filled with LY more rapidly than with Alexa488 (compare Figs. 2 and 5). This finding, of course, simply reflects the fact that the aqueous diffusion constant of LY is larger than Alexa488 because of their size difference.

The spatial patterns of fluorescence intensity measured in three different COS loaded with LY are illustrated in Fig. 6 (*symbols*). For each cell, we show spatial patterns measured at various times after achieving WCM, a moment we define as time 0. To match experimental and computational results, the COS tip is assigned as the origin of the spatial variable. In Fig. 6 we show as continuous curves computed fluorescence spatial patterns that best matched our experimental data. In Fig. 6, A–C, the curves are solutions of the reduced diffusion equation for a fixed value of δ selected to best fit the experimental results. We obtained reasonably good matches between experimental and computational data, and the results in Fig. 6 illustrate the range of the quality of the fits.

In Table 2 we detail the features of LY diffusion in six different cone outer segments. The analysis points out that the value of the longitudinal diffusion coefficient varies with position along the COS length. This feature is highlighted by presenting the value of the diffusion coefficient at the COS base and tip. Despite the difference in the value of diffusion coefficients, LY diffusion yields a value for the equivalent diameter δ that is essentially the same as that derived from Alexa488 diffusion (Tables 1 and 2). This verifies that neither fluorophore binds to intracellular sites and their diffusional motion reflects the same mechanical hindrance, imposed by the COS structure.

Anatomical determination of the equivalent diameter δ

For both Alexa488 and LY, diffusional flux between adjacent COS folds is well described as occurring across

TABLE 1 Cytoarchitecture and the longitudinal diffusion of Alexa488 in bass single cone outer segments

Single COS	COS dimensions (μm)			$\bar{\delta}_a$ (μm)	δ (μm)	L_h (μm)	L_h/L	D_{base} $\mu\text{m}^2/\text{s}$	D_{tip} $\mu\text{m}^2/\text{s}$	$D_{\text{base}}/D_{\text{tip}}$
	Length L	Base radius	Tip radius							
108_1	16.1	2.77	1.08	0.346	0.316	8.53	0.53	2.6	16.7	6.5
108_4	15	3.38	1.22	0.376	0.330	7.20	0.48	1.9	14.4	7.6
124_3	16.57	3.43	1.36	0.388	0.316	8.61	0.52	1.7	10.7	6.3
129_3	13.52	3.15	1.30	0.376	0.346	6.48	0.48	2.4	13.9	5.8
129_6	13.48	3.34	1.39	0.388	0.316	6.99	0.52	1.8	10.2	5.7
1227_1	14.18	3.35	1.27	0.378	0.324	7.51	0.53	1.9	12.8	6.9
Mean \pm SD	14.81 \pm 1.31	3.23 \pm 0.25	1.27 \pm 0.11	0.376 \pm 0.016	0.325 \pm 0.012	7.56 \pm 0.85	0.51 \pm 0.02	2.05 \pm 0.36	13.12 \pm 2.43	6.5 \pm 0.7

$\bar{\delta}_a$ is the mean anatomical equivalent diameter of surface connecting adjacent membrane folds; δ is the mean diffusion equivalent diameter of surface connecting adjacent membrane folds; and L_h is the longitudinal position where COS taper changes.

the surface of an equivalent circle, whose diameter δ can be known from the fit between experimental and computational data. In our results, the mean δ was $0.325 \pm 0.012 \mu\text{m}$ for Alexa488 and $0.324 \pm 0.025 \mu\text{m}$ for LY (Tables 1 and 2). In reality, the surface connecting adjacent folds is not circular; rather, it is a semicircular torus that surrounds one-half the perimeter of the membrane folds over the entire COS length (Fig. 1) (Fetter and Corless, 1987). If longitudinal diffusion is indeed determined by the COS architecture, then the computed equivalent surface should be the same as the true anatomical surface area.

The anatomical surface area of diffusion can be computed as described in A Theory of Longitudinal Diffusion to yield an anatomical average diameter $\bar{\delta}_a$. Tables 1 and 2 present the computed $\bar{\delta}_a$ and δ -values for both Alexa488 and LY in every cell analyzed. The two numbers are remarkably similar. The small, $\sim 10\%$, but consistent difference between them can be resolved by simply assigning the fraction of the fold's perimeter surrounded by plasma membrane to be 0.4, rather than the stipulated 0.5. Anatomical studies have only approximated the extent of surface draping, and precise morphometric data to resolve the issue do not exist. The similarity in the values of $\bar{\delta}_a$ and δ confirms the validity of

the diffusion analysis and offers a specific structural insight to the value of δ . The quantitative similarity of results arrived at through independent investigation of both Alexa488 and LY affirms the assumption that these fluorescent molecules do not bind in the COS cytoplasm; their molecular movement can be fully described as Brownian motion restricted only by the photoreceptor's cellular architecture.

DISCUSSION

We have developed a theoretical analysis to compute the cytoplasmic longitudinal diffusion constant, D_1 in rod and $D_1(x)$ cone outer segments. The value of the diffusion constant depends only on the aqueous diffusion constant of the molecule and the details of the outer segment's structure. The analysis envisions that molecules diffuse between adjacent rod disks or cone membrane folds through a surface defined as an equivalent circle of diameter δ . The value of this diameter can be computed from experimental measurements of longitudinal diffusion or from known anatomical OS features, yielding an anatomical equivalent diameter $\bar{\delta}_a$. We measured the longitudinal diffusion of Alexa488 and LY in single bass COS and analyzed the experimental data with our

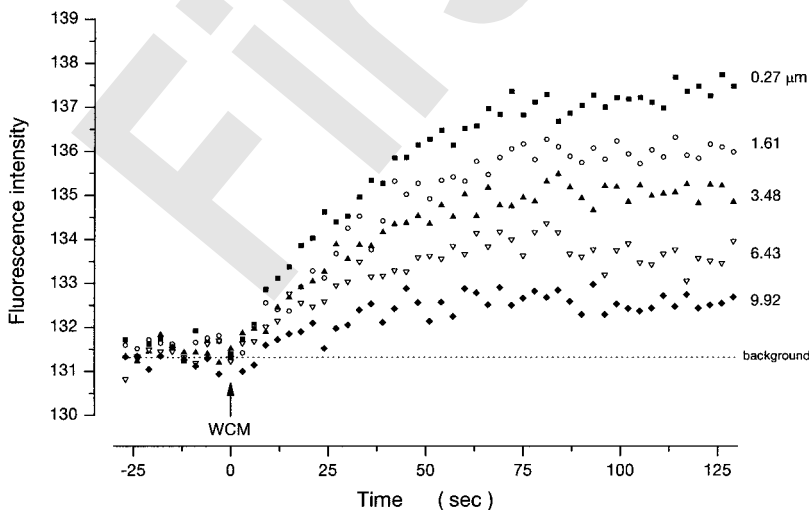


FIGURE 5 Time course of single COS filling with lucifer yellow. COS dimensions were length = $16.39 \mu\text{m}$, base diameter = $6.74 \mu\text{m}$, and tip diameter = $2.62 \mu\text{m}$. Fluorescence intensity was measured using a sampling grid consisting of 61 elements placed adjacent to each other over the entire COS length (see Materials and Methods). Each element was $7.03 \mu\text{m}$ in the transverse axis by $0.27 \mu\text{m}$ in the longitudinal one, and laid perpendicular to the COS longitudinal axis. Before achieving WCM (designated as $t = 0$) COS fluorescence intensity was the same as background; after WCM, fluorescence intensity increased steadily, first at the COS base and eventually at its tip, revealing the longitudinal flux of lucifer yellow.

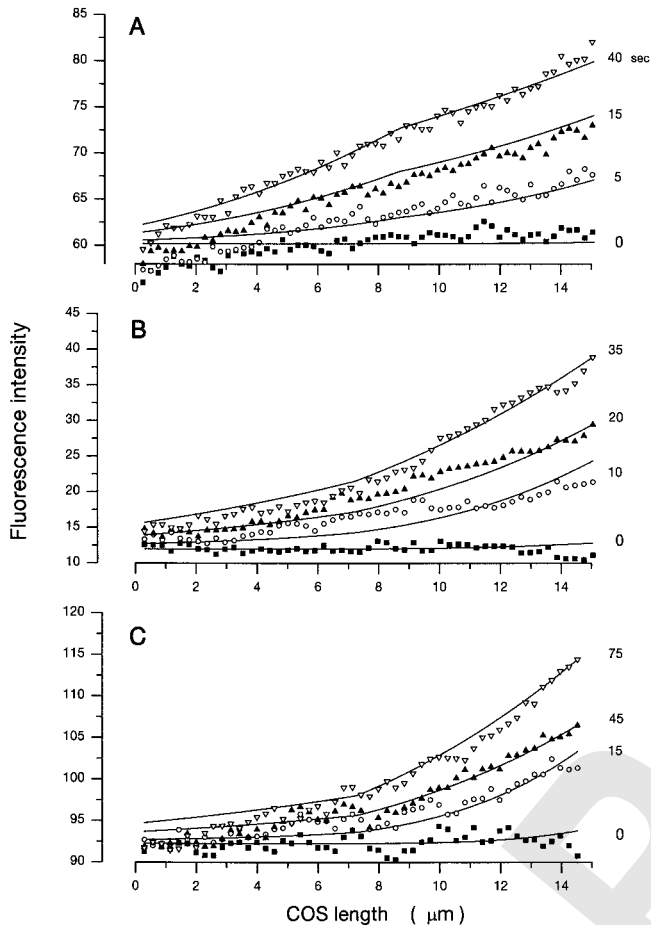


FIGURE 6 Spatial pattern of fluorescence intensity at various times after the start of LY diffusion into single bass COS. Data measured in three different cells are shown. (A) The COS dimensions were length = 14.64 μm , base diameter = 6.32 μm , and tip diameter = 2.10 μm . Fluorescence was sampled with a grid consisting of 51 elements, each 6.4 μm in the transverse axis by 0.29 μm in the longitudinal one. (B) The COS dimensions were length = 15.1 μm , base diameter = 5.52 μm , and tip diameter = 2.06 μm . Fluorescence was sampled with a grid consisting of 51 elements, each 5.5 μm in the transverse axis by 0.30 μm in the longitudinal one. (C) The COS dimensions were length = 17.37 μm , base diameter = 6.88 μm , and tip diameter = 2.26 μm . Fluorescence was sampled with a grid consisting of 68 elements, each 6.9 μm in the transverse axis by 0.26 μm in the longitudinal one. The continuous curves are solutions of the geometrical reduction of the diffusion equation we have derived (see A Theory of Longitudinal Diffusion). The lines describe Alexa concentration as a function of cell longitudinal position, each at a fixed time (as labeled), where $t = 0$ is the moment WCM is achieved and diffusion begins. Values of the adjustable parameters that generated the curves: (A) $\delta = 0.316 \mu\text{m}$ (the equivalent radius of the circular surface that joins adjacent COS folds) and $L_h = 7.32 \mu\text{m}$ (the location of the taper transition point); (B) $\delta = 0.340 \mu\text{m}$ and $L_h = 7.24 \mu\text{m}$; and (C) $\delta = 0.330 \mu\text{m}$ and $L_h = 8.69 \mu\text{m}$.

method of theoretical analysis. The mean value of δ and δ_a in the bass cone is the same, $\sim 0.325 \mu\text{m}$ (Tables 1 and 2), and measurements with either Alexa488 or LY yield the same result. These findings verify that the method of analysis is robust and can be used to study the longitudinal diffusion of

hydrophilic molecules of interest, provided they do not bind and are small enough to diffuse within the outer segment.

The analytical method also applies to ROS, where it envisions that molecules diffuse between adjacent interdisk spaces through disk incisures and the gap that separates disks from the plasma membrane. The validity of the analysis to study longitudinal diffusion in ROS is confirmed by the fact that the theoretically computed value of D_1 for cGMP in tiger salamander rods overlaps experimentally determined ones (Table 3). Moreover, the D_1 value for Alexa488 theoretically computed for tiger salamander ROS ($14.5 \mu\text{m}^2 \text{s}^{-1}$) is similar to that determined experimentally ($16 \mu\text{m}^2 \text{s}^{-1}$) by measuring the spatial pattern of fluorescence in isolated rods loaded with the dye using the same method described here for cones (our unpublished results).

Longitudinal diffusion of cGMP in rod and cone outer segments of similar dimensions

cGMP longitudinal diffusion determines the quantitative features of the spread of photoexcitation over the outer segment length away from the site of photon capture. Spread of photoexcitation in ROS has been measured experimentally in a number of reports (Hagins et al., 1970; Hemila and Reuter, 1981; Lamb et al., 1981; Matthews, 1986; Gray-Keller et al., 1999). Results indicate that, at the peak of the photocurrent, signals spread to $1/e$ of its peak amplitude over distances of between 5 and 15 μm . These values are, at best, upper bounds on the true range of the signal spread because, as discussed in the reports, light scattering makes it impossible to restrict excitation to only a single disk (Hagins et al., 1970; Hemila and Reuter, 1981; Lamb et al., 1981; Matthews, 1986). The elegant use of two-photon excitation by Gray-Keller et al. (1999) has reduced this experimental uncertainty and they report that in Gecko ROS and at the peak of the photocurrent (~ 1 s after a flash), cGMP concentration declines to $1/e$ of its maximum value over $\sim 3.5 \mu\text{m}$. Experimental assessment of spatial spread of cGMP in cones has not been reported.

We applied the theoretical analysis to investigate longitudinal diffusion of cGMP in ROS and COS. In our simulations, we assume cGMP movement is only restricted by cytoarchitecture and not by binding. Although the nucleotide binds to noncatalytic sites in the photoreceptor's phosphodiesterase (PDE) (Mou et al., 1999), their affinity is so high (nM) that the sites are saturated at the μM concentrations expected in dark-adapted photoreceptors. Also, cGMP-gated ion channels bind cGMP, but the concentration of channels at the sites of diffusion is negligible. The dominant effect of binding to channels or PDE is reflected in the transverse diffusion. We present in Tables 3 and 4 computed D_1 values of cGMP in ROS and COS (at midlength) of several species in which outer segment structure is known in detail.

TABLE 2 Cytoarchitecture and the longitudinal diffusion of lucifer yellow in bass single cone outer segments

Single COS	COS dimensions (μm)			$\bar{\delta}_a$ (μm)	δ (μm)	L_h (μm)	L_h/L	D_{base} $\mu\text{m}^2/\text{s}$	D_{tip} $\mu\text{m}^2/\text{s}$	$D_{\text{base}}/D_{\text{tip}}$
	Length L	Base radius	Tip radius							
212_2	16.39	3.37	1.31	0.382	0.360	8.20	0.5	2.4	15.9	6.5
219_3	13.25	3.05	1.37	0.378	0.282	6.36	0.48	1.8	9.0	4.9
225_1	15.08	2.76	1.03	0.342	0.340	7.24	0.48	3.3	22.8	7
303_3	14.64	3.16	1.05	0.356	0.316	7.32	0.50	2.1	19	8.8
303_1	17.37	3.44	1.13	0.370	0.330	8.69	0.50	2.0	17.9	9.0
303_2	14.55	2.70	1.03	0.340	0.316	7.28	0.50	2.9	19.7	6.7
Mean \pm SD	15.21 \pm 1.46	3.08 \pm 0.31	1.15 \pm 0.15	0.362 \pm 0.018	0.324 \pm 0.025	7.51 \pm 0.82	0.49 \pm 0.01	2.4 \pm 0.6	17.4 \pm 4.7	7.15 \pm 1.5

$\bar{\delta}_a$ is the mean anatomical equivalent diameter of surface connecting adjacent membrane folds; δ is the mean diffusion equivalent diameter of surface connecting adjacent membrane folds; and L_h is the longitudinal position where COS taper changes.

To evaluate the spread of cGMP over the length of ROS and COS, its concentration was simulated by imposing an absorbing boundary condition at a given location. This absorbing boundary condition reproduces the instantaneous depletion of cGMP concentration within an active compartment, as would be caused by light-dependent activation of phosphodiesterase. After hydrolysis begins, and in the absence of metabolic replenishment, cGMP concentration decreases throughout the OS as the nucleotide diffuses into the active compartment and is instantly hydrolyzed. The cytoplasmic cGMP concentration is the solution of the PDE,

$$\frac{\partial c}{\partial t} = D_{\text{long}}(x) \frac{\partial^2 c}{\partial x^2} \quad \text{on } [0, L], \quad (46)$$

under the initial conditions of

$$c(x, 0) = C_0, \quad \text{on } [0, L] - [a_1, b_1] \quad (47)$$

$$c(x, 0) = 0, \quad \text{on } [a_1, b_1]. \quad (48)$$

Since the cGMP cannot escape from the OS, the boundary conditions are

$$\frac{\partial c}{\partial x}(0, t) = \frac{\partial c}{\partial x}(L, t) = 0, \quad (49)$$

where L is the total OS length, C_0 is the steady-state cGMP concentration, and the depleted compartment is $[a_1, b_1]$.

In Fig. 7 we illustrate the simulated time course of the cGMP cytoplasmic concentration for human rods and cones. Shown are simulations of the expected spatial pattern of cGMP concentration loss in OS caused by continuous cGMP hydrolysis in a single compartment. cGMP destruction in the active compartment starts at time 0 and is sustained for different periods, as labeled. We elected to compare human rods and cones because they are rather similar in size (Tables 3 and 4) and their cGMP concentration in the dark can be reasonably estimated. Considering that $\sim 2\%$ of the cGMP-gated channels are active in darkness and given the known Hill equation relationship between channel activity and cGMP concentration (Dhallan et al., 1992; Wissinger et al., 1997; Peng et al., 2003), the nucleotide concentration in human ROS is $\sim 17 \mu\text{M}$ (270 cGMP molecules/compartment) and $4.3 \mu\text{M}$ in cones (59 cGMP molecules/compartment at the tip and 189 at the base). To compare rods and cones, we explored periods of hydrolysis proportional to

TABLE 3 Comparison of predicted and experimental values of cGMP longitudinal diffusion constant in rod outer segments

Species	ROS structure			cGMP diffusion			
	Length (μm)	Diameter (μm)	No. incisures	D_{aq} ($\mu\text{m}^2/\text{s}$)	D_1 (exp.) ($\mu\text{m}^2/\text{s}$)	D_1 (theory) ($\mu\text{m}^2/\text{s}$)	λ_{rod} (μm)
Tiger salamander	25.3*	12.3	18 [†]	500	30–60 [‡] 1–11 [†]	18.5	4.7 [§]
Striped bass [¶]	40	1.6	1			41.6	3.8 [¶]
Human, peripheral retina	12	1.5	1			44.3	3.0**
Guinea pig ^{††}	5	1.4	1			47.3	
Rat ^{‡‡}	25	1.7	1			39.3	

*Our data, $n = 11$.

[†]Olson and Pugh (1993).

[‡]Koutalos et al. (1995a,b).

[§]Miller and Korenbrot (1993); $t_p = 1.2 \text{ s}$ at 20°C .

[¶]Miller and Korenbrot (1993); $t_p = 340 \text{ ms}$ at 20°C .

^{||}Kolb et al. (2003); WebVision. <http://retina.umh.es/Webvision/>.

**Schneeweis and Schnapf (1999); $t_p = 200 \text{ ms}$ at 37°C .

^{††}Clark and Branton (1968).

^{‡‡}Pedler and Tilly (1967).

TABLE 4 Computational predictions of the cGMP longitudinal diffusion constant and characteristic spread space constant in cone outer segments

Species	COS structure			cGMP diffusion				
	Length (μm)	Base radius (μm)	Tip radius (μm)	δ (μm)	D_1 (base) ($\mu\text{m}^2/\text{s}$)	D_1 (tip) ($\mu\text{m}^2/\text{s}$)	D_1 (at $L/2$) ($\mu\text{m}^2/\text{s}$)	λ_{cone} (at $L/2$) (μm)
Striped bass, single cone	15	3.1	1.2	0.324*	2.7	17.9	5.6	0.79 [†]
Tiger salamander, single cone	8.5	2.5	1.1	0.314 [‡]	3.9	20.0	7.6	0.99 [§]
Human, peripheral retina [¶]	7	1.5	0.75	0.244 [‡]	6.6	25.8	11.6	0.68

*Experimental data from Tables 1 and 2.

[†]Miller and Korenbrot (1993); $t_p = 110$ ms at 20°C.

[‡]Computed δ_a .

[§]Miller et al. (1994); $t_p = 130$ ms at 20°C.

[¶]Kolb et al. (2003); WebVision. <http://retina.umh.es/Webvision/>.

^{||}Schnapf, et al. (1990) and Schneeweis and Schnapf (1999); $t_p = 40$ ms at 37°C.

the cell's photocurrent time to peak (t_p). For both photoreceptors, the curves shown were computed for 0.2 t_p (red), 0.4 t_p (blue), 0.6 t_p (green), 0.8 t_p (orange), and t_p (gray). On average, t_p at 37°C are 200 ms in human rods and 40 ms in cones (Baylor et al., 1984; Schnapf et al., 1990; Kraft et al., 1993; Schneeweis and Schnapf, 1999).

Examination of the data in Fig. 7 shows that the spatial pattern of cGMP spread in COS changes with the location of the active compartment. The pattern is broader at the base than the tip, and it is asymmetric at either location. In rods the pattern is symmetric and identical at any location, although for convenience of illustration we selected a com-

partment in the middle of the ROS. Of particular relevance is that, for a fixed duration of hydrolysis (e.g., 40 ms), the spatial pattern differs significantly between the receptor types: it is far broader in the ROS than the COS.

Spatial spread constant of cGMP in ROS and COS: comparison across species

As an additional means to compare longitudinal cGMP spread in ROS and COS across species, we define a spread space constant λ as follows (Eqs. 33 and 35):

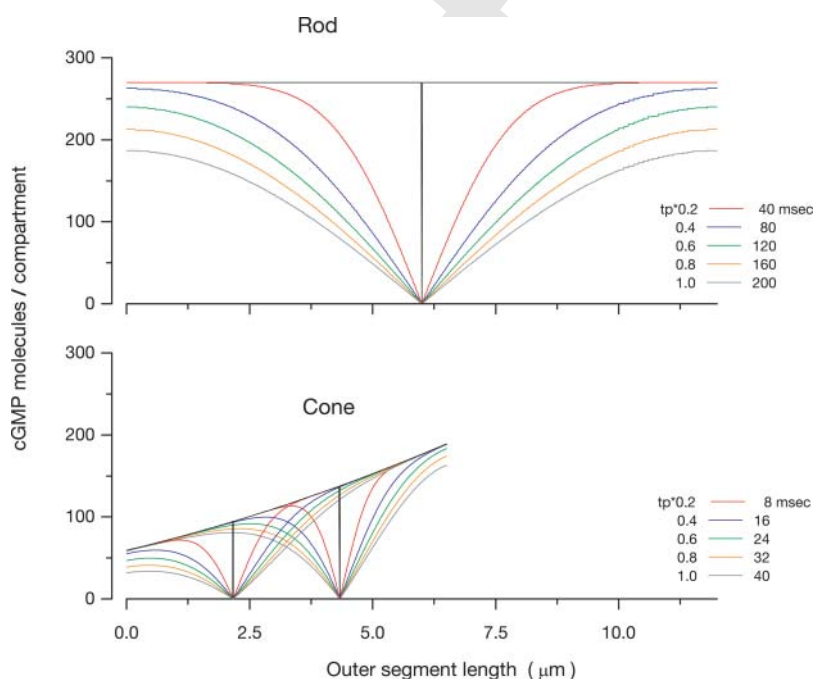


FIGURE 7 Computed spread of cGMP loss in human rod and cone outer segments. Shown are simulations of the expected spatial pattern of cGMP concentration decrease in outer segments caused by active destruction of the nucleotide in a single interdisk or membrane folding. cGMP destruction in the active compartment start at $time = 0$ and is sustained for different time periods. The periods selected are scaled with the time to peak of the dim-light photocurrent in the cells. For both photoreceptors, the curves shown were computed for 20% (red), 40% (blue), 60% (green), 80% (orange), and 100% (gray) of the time to peak. Since the mean times to peak at 37°C are 200 ms in rods and 40 ms in cones, the families of curves at each location depict the spatial pattern in rods 40, 80, 120, 160, and 200 ms after cGMP hydrolysis begins and in cones at 8, 16, 24, 32, and 40 ms. cGMP concentration is expressed as number of particles per spatial compartment, U_k (see A Theory of Longitudinal Diffusion). The outer segment tip is designated as the origin of the length axis ($x = 0$). Although the outer segments are of comparable dimensions, the concentration spread at the same time is far broader in rods than in cones. Moreover, the spatial spread in rods is symmetric with respect to the active compartment and is the same for any longitudinal location of the active compartment. In cones, in contrast, the spread is not symmetric and the spatial patterns depend on the initial location of the active compartment. These differences are consequences of the distinct cytoarchitecture of rod and cone outer segments and the initial cGMP concentration.

$$\lambda_{\text{rod}} = \sqrt{D_1 t_p}$$

$$\lambda_{\text{cone}}(x) = \sqrt{D_1(x) t_p}$$

Under some simplifying assumptions (see A Theory of Longitudinal Diffusion), λ_{rod} is the standard deviation of the diffusion process at time t_p at any position along the OS length; $\lambda_{\text{cone}}(x)$ is the standard deviation of the diffusion process at t_p at a specific location x along the COS length.

Let us first compare rods and cones of similar dimensions. In human rods, $\lambda_{\text{rod}} = 3 \mu\text{m}$. In human cones, at a point one-third the length of the OS, near the base, $D_1 = 9.4 \mu\text{m}^2 \text{s}^{-1}$ and $\lambda_{\text{con}} = 0.61 \mu\text{m}$. At a point two-thirds the length of the OS, near the tip, $D_1 = 14.6 \mu\text{m}^2 \text{s}^{-1}$ and $\lambda_{\text{con}} = 0.76 \mu\text{m}$. That is, the combination of a more limited cGMP diffusional flux and a faster photocurrent kinetics should, at the peak of the photoresponse, cause cGMP to spread only one-fifth as far in COS as in ROS of comparable size.

We extended the computation of λ to rods and cones of several species in which both cell anatomy and physiology are known. Results are collected in Tables 3 and 4. It is remarkable to us that the longitudinal spread of cGMP is consistently smaller in cones than rods across all species, but even more so, that the magnitude of the spread is relatively the same in all rods ($\lambda_{\text{rod}} 3\text{--}5 \mu\text{m}$) and in all cones ($\lambda_{\text{con}} 0.7\text{--}0.9 \mu\text{m}$) regardless of their absolute size. This finding suggests that longitudinal diffusion is of such functional significance that evolutionary pressures have optimized the relationship between the gross dimensions of the OS and the detailed features of its ultrastructure in order to maintain the cGMP spread space constant as nearly invariant and independent of the OS absolute dimensions.

Role of longitudinal diffusion in the continuous component of dark noise

The current across the outer segment membrane fluctuates in darkness and light suppresses this fluctuation. This continuous dark noise differs in extent in rods and cones of the same species. In primates, for example, the root mean-square amplitude of the noise is $\sim 0.03 \text{ pA}$ in rods (Baylor et al., 1984), whereas it is 0.12 pA in cones (Schnapf et al., 1990). The dark noise has been attributed to fluctuations in the number of active PDEs (Rieke and Baylor, 1996). Since there are ~ 1000 compartments in a single OS, if every compartment acted independently, dark current noise should be much smaller than is observed because of statistical averaging over the large number of compartments; observed noise would be compartmental noise divided by square-root of the number of compartments. The fact that significant dark noise is detected suggests that individual compartments are not independent, but functionally coupled. This coupling is likely mediated by cGMP longitudinal diffusion. Changes in cGMP within a single compartment, caused by local PDE

activity, must inevitably result in a cGMP concentration gradient along the OS and cGMP flux between compartments. This local longitudinal flux, and the consequent recruitment of neighboring compartments, likely explains the finding that dark noise variance increases linearly with OS length (Baylor et al., 1980). The differences in longitudinal diffusion between rods and cones must be considered in any mechanism that seeks to explain the differences in dark current noise between photoreceptor types.

APPENDIX

Short-term asymptotic solution of the longitudinal diffusion solution in cone outer segments

In this Appendix, we provide an explicit computation of the solution of the cone diffusion equation, in the short time asymptotic limit. No explicit solution is available, and the computation is derived for large length L . We use the standard WKB method (Schuss, 1980).

The computation is as follows. Equation 22 is first transformed into a dimensionless equation by scaling the variables. The new function, v , defined by

$$v(x, t) = c \left(\frac{r}{d} x, \frac{t}{2D} \right), \quad (\text{A1})$$

satisfies the PDE

$$\frac{\partial v}{\partial t}(\mathbf{x}, t) = \frac{1}{1+x^2} \frac{\partial^2 v}{\partial \mathbf{x}^2}(\mathbf{x}, t), \quad (\text{A2})$$

$$v(\mathbf{x}, 0) = \delta_0. \quad (\text{A3})$$

To find the asymptotic, we use the Laplace transform of the equation. Denoting the Laplace transform in the t -variable by \hat{v} ,

$$\hat{v}(p, x) = \int_0^{+\infty} e^{-pt} v(x, t) dt,$$

Eq. A2 becomes

$$p\hat{v} - \delta_0 = \frac{1}{1+x^2} \frac{\partial^2 \hat{v}}{\partial \mathbf{x}^2}(\mathbf{x}, p). \quad (\text{A4})$$

To compute the general solution of

$$p\hat{v} = \frac{1}{1+x^2} \frac{\partial^2 \hat{v}}{\partial \mathbf{x}^2}(\mathbf{x}, p), \quad (\text{A5})$$

such that $v(x, t) \rightarrow \delta_0$ as t goes to 0 , we have considered the asymptotic p goes to infinity. In the WKB approximation (Schuss, 1980), the first term in the approximation of \hat{u} is of the form

$$\hat{v}(p, x) = \frac{Q(x)}{\sqrt{P}} e^{-\frac{P(x)}{\sqrt{P}}}, \quad (\text{A6})$$

where P and Q are two functions to be determined. To determine explicitly these two functions, the approximated solution \hat{u} from Eq. A6 is substituted

in Eq. A5, and by equating the term in the variable $1/\sqrt{p}$, we recover that the function P is the solution of the Eikonal equation,

$$P'(x)^2 = 1 + x^2. \quad (\text{A7})$$

Since we are interested in solutions that are decaying as x goes to infinity, we choose

$$P'(x) = -\sqrt{1 + x^2}, \quad (\text{A8})$$

and after integration, to an additive constant, we obtain that

$$P(x) = \frac{x\sqrt{1+x^2}}{2} + \frac{1}{2}\log(x + \sqrt{1+x^2}). \quad (\text{A9})$$

The second term in the asymptotic leads to the transport equation

$$2P_x Q_x + Q P_{xx} = 0, \quad (\text{A10})$$

and the solution is

$$Q(x) = \frac{1}{\sqrt{P_x}} = \frac{1}{(1+x^2)^{1/4}}. \quad (\text{A11})$$

From

$$\hat{v}(p, x) = \frac{1}{\sqrt{p}} \left(\frac{1}{(1+x^2)^{1/4}} + O(p^{-1/2}) \right) e^{-\frac{P(x)}{\sqrt{p}}}, \quad (\text{A12})$$

and recalling that the inverse Laplace transform,

$$L^{-1} \left(\frac{1}{\sqrt{p}} e^{-\sqrt{p}P(x)} \right) = \frac{1}{\sqrt{t\pi}} e^{-\frac{P^2(x)}{4t}}, \quad (\text{A13})$$

as t goes to 0, we obtain that

$$u(t, x) \sim_{t \rightarrow 0} \left(\frac{1}{(1+x^2)^{1/4}} + O(t^{1/2}) \right) \frac{1}{2t^{1/2}\sqrt{\pi}} e^{-\frac{P^2(x)}{4t}}; \quad (\text{A14})$$

and transforming back to the initial equation, the leading term of the solution of the diffusion equation for cone is

$$c(t, x) \sim_{t \rightarrow 0} \left(\frac{\delta^2}{(\delta^2 + (dx + d_0)^2)^{1/4}} \right) \times \frac{1}{2\sqrt{2\pi Dt}} e^{-(p^2(d/\delta)x + (d_0/\delta))/8Dt}, \quad (\text{A15})$$

where

$$P \left(\frac{d}{\delta}x + \frac{d_0}{\delta} \right) = \frac{\frac{d}{\delta}x + \frac{d_0}{\delta} + \sqrt{1 + \left(\frac{d}{\delta}x + \frac{d_0}{\delta} \right)^2}}{2} + \frac{1}{2} \log \left(\frac{d}{\delta}x + \frac{d_0}{\delta} + \sqrt{1 + \left(\frac{d}{\delta}x + \frac{d_0}{\delta} \right)^2} \right).$$

From Eq. A15, the fundamental solution decays exponentially but note the difference with the solution of the fundamental solution of the rod diffusion equation (with a coefficient constant equal to $2D$), given by

$$c(t, x) = \frac{1}{2\sqrt{2\pi Dt}} e^{-\frac{x^2}{8Dt}}. \quad (\text{A16})$$

We thank M. P. Faillace and N. Rouach for their valuable comments on the manuscript.

D.H. gratefully acknowledges financial support from the Sloan-Swartz Foundation. Research was supported by National Institutes of Health grant EY05498.

REFERENCES

- Barnes, S., and B. Hille. 1989. Ionic channels of the inner segment of tiger salamander cone photoreceptors. *J. Gen Physiol.* 94:719–743.
- Baylor, D. A., G. Matthews, and K. W. Yau. 1980. Two components of electrical dark noise in toad retinal rod outer segments. *J. Physiol. (Lond.)* 309:591–621.
- Baylor, D. A., B. J. Nunn, and J. L. Schnapf. 1984. The photocurrent, noise and spectral sensitivity of rods of the monkey *macaca fascicularis*. *J. Physiol. (Lond.)* 357:575–607.
- Blaurock, A. E., and M. H. Wilkins. 1969. Structure of frog photoreceptor membranes. *Nature*. 223:906–909.
- Borwein, B. 1981. The retinal receptors: a description. In *Vertebrate Photoreceptor Optics*. J. M. Enoch and F. L. Tobey, editors. Springer-Verlag, Berlin, Germany. 11–82.
- Bowen, W. J., and H. L. Martin. 1964. The diffusion of adenosine triphosphate through aqueous solution. *Arch. Biochem. Biophys.* 107:30–36.
- Clark, A. W., and D. Branton. 1968. Fracture faces in frozen outer segments from the guinea pig retina. *Z. Zellforsch. Mikrosk. Anat.* 91:586–603.
- Cohen, A. I. 1968. New evidence supporting the linkage to extracellular space of outer segment saccules of the frog cones but not rods. *J. Cell Biol.* 37:424–437.
- Dhallan, R. S., J. P. Macke, R. L. Eddy, T. B. Shows, R. R. Reed, K. W. Yau, and J. Nathans. 1992. Human rod photoreceptor cGMP-gated channel: amino acid sequence, gene structure, and functional expression. *J. Neurosci.* 12:3248–3256.
- Fetter, R. D., and J. M. Corless. 1987. Morphological components associated with frog cone outer segment disk margins. *Invest. Ophthalmol. Vis. Sci.* 28:646–657.
- Gray-Keller, M., W. Denk, B. Shraiman, and P. B. Detwiler. 1999. Longitudinal spread of second messenger signals in isolated rod outer segments of lizards. *J. Physiol.* 519:679–692.
- Hagins, W. A., R. D. Penn, and S. Yoshikami. 1970. Dark current and photocurrent in retinal rods. *Biophys. J.* 10:380–412.

- Hagins, W. A., and H. Ruppel. 1971. Fast photoelectric effects and the properties of vertebrate photoreceptors as electric cables. *Fed. Proc.* 30:64–68.
- Hemila, S., and T. Reuter. 1981. Longitudinal spread of adaptation in the rods of the frog's retina. *J. Physiol.* 310:501–528.
- Hestrin, S., and J. I. Korenbrot. 1987. Effects of cyclic GMP on the kinetics of the photocurrent in rods and in detached rod outer segments. *J. Gen. Physiol.* 90:527–551.
- Hochstrate, P., and H. Ruppel. 1980. On the evaluation of photoreceptor properties by micro-fluorimetric measurements of fluorochrome diffusion. *Biophys. Struct. Mech.* 6:125–138.
- Januschka, M. M., D. A. Burkhardt, S. L. Erlandsen, and R. L. Purple. 1987. The ultrastructure of cones in the walleye retina. *Vision Res.* 27:327–341.
- Knabe, W., and H. Kuhn. 1998. Disk formation in retinal cones of *Tupaia belangeri* (Scandentia). *Cell Tissue Res.* 292:67–76.
- Korenbrot, J. I., D. T. Brown, and R. A. Cone. 1973. Membrane characteristics and osmotic behavior of isolated rod outer segments. *J. Cell Biol.* 56:389–398.
- Koutalos, Y., R. L. Brown, J. W. Karpen, and K. W. Yau. 1995a. Diffusion coefficient of the cyclic GMP analog 8-(fluoresceinyl)thioguanosine 3',5' cyclic monophosphate in the salamander rod outer segment. *Biophys. J.* 69:2163–2167.
- Koutalos, Y., K. Nakatani, and K. W. Yau. 1995b. Cyclic GMP diffusion coefficient in rod photoreceptor outer segments. *Biophys. J.* 68:373–382.
- Kraft, T. W., D. M. Schneeweis, and J. L. Schnapf. 1993. Visual transduction in human rod photoreceptors. *J. Physiol. (Lond.)* 464:747–765.
- Lamb, T. D., P. A. McNaughton, and K. W. Yau. 1981. Spatial spread of activation and background desensitization in toad rod outer segments. *J. Physiol.* 319:463–496.
- Laties, A. M., and P. A. Liebman. 1970. Cones of living amphibian eye: selective staining. *Science.* 168:1475–1477.
- Leeson, T. S. 1970. Rat retinal rods: freeze-fracture replication of outer segments. *Can. J. Ophthalmol.* 5:91–107.
- Maricq, A. V., and J. I. Korenbrot. 1990. Potassium currents in the inner segment of single retinal cone photoreceptors. *J. Neurophysiol.* 64:1929–1940.
- Matthews, G. 1986. Spread of the light response along the rod outer segment: an estimate from patch-clamp recordings. *Vision Res.* 26:535–541.
- McLaughlin, S., and J. Brown. 1981. Diffusion of calcium ions in retinal rods. A theoretical calculation. *J. Gen. Physiol.* 77:475–487.
- Miller, J. L., and J. I. Korenbrot. 1993. Phototransduction and adaptation in rods, single cones, and twin cones of the striped bass retina: a comparative study. *Vis. Neurosci.* 10:653–667.
- Miller, J. L., A. Picones, and J. I. Korenbrot. 1994. Differences in transduction between rod and cone photoreceptors: an exploration of the role of calcium homeostasis. *Curr. Opin. Neurobiol.* 4:488–495.
- Mou, H., H. J. Grazio 3rd, T. A. Cook, J. A. Beavo, and R. H. Cote. 1999. cGMP binding to noncatalytic sites on mammalian rod photoreceptor phosphodiesterase is regulated by binding of its gamma and delta subunits. *J. Biol. Chem.* 274:18813–18820.
- Nakatani, K., C. Chen, and Y. Koutalos. 2002. Calcium diffusion coefficient in rod photoreceptor outer segments. *Biophys. J.* 82:728–739.
- Nilsson, S. E. 1964. Receptor cell outer segment development and ultrastructure of the disk membranes in the retina of the tadpole (*Rana pipiens*). *J. Ultrastruct. Res.* 11:581–602.
- Nilsson, S. E. 1965. The ultrastructure of the receptor outer segment in the retina of the leopard frog (*Rana pipiens*). *J. Ultrastruct. Res.* 12:207–225.
- Ohyama, T., D. H. Hackos, S. Frings, V. Hagen, U. B. Kaupp, and J. I. Korenbrot. 2000. Fraction of the dark current carried by Ca^{2+} through CGMP-gated ion channels of intact rod and cone photoreceptors. *J. Gen. Physiol.* 116:733–754.
- Olson, A., and E. N. Pugh, Jr. 1993. Diffusion coefficient of cyclic GMP in salamander rod outer segments estimated with two fluorescent probes. *Biophys. J.* 65:1335–1352.
- Pedler, C. M., and R. Tilly. 1967. The fine structure of photoreceptor disks. *Vision Res.* 7:829–836.
- Peng, C., E. D. Rich, C. A. Thor, and M. D. Varnum. 2003. Functionally important calmodulin-binding sites in both NH_2 and $COOH$ terminal regions of the cone photoreceptor cyclic nucleotide-gated channel CNGB3 subunit. *J. Biol. Chem.* 278:24617–24623.
- Picones, A., and J. I. Korenbrot. 1992. Permeation and interaction of monovalent cations with the cGMP-gated channel of cone photoreceptors. *J. Gen. Physiol.* 100:647–673.
- Pugh, E. N., Jr., and T. D. Lamb. 2000. Phototransduction in vertebrate rods and cones: molecular mechanisms of amplification, recovery and light adaptation. In *Handbook of Biological Physics*, Vol. 3. Elsevier Science, Amsterdam. 186–255.
- Rieke, F., and D. A. Baylor. 1996. Molecular origin of continuous dark noise in rod photoreceptors. *Biophys. J.* 71:2553–2572.
- Rispoli, G., W. A. Sather, and P. B. Detwiler. 1993. Visual transduction in dialysed detached rod outer segments from lizard retina. *J. Physiol. (Lond.)* 465:513–537.
- Roof, D. J., and J. E. Heuser. 1982. Surfaces of rod photoreceptor disk membranes: integral membrane components. *J. Cell Biol.* 95:487–500.
- Rosenkranz, J. 1970. On the fine structure of the frog's rod outer segments, observed by the freeze-etching technique. *Z. Zellforsch. Mikrosk. Anat.* 111:228–262.
- Schnapf, J. L., B. J. Nunn, M. Meister, and D. A. Baylor. 1990. Visual transduction in cones of the monkey *macaca fascicularis*. *J. Physiol. (Lond.)* 427:681–713.
- Schneeweis, D. M., and J. L. Schnapf. 1999. The photovoltage of macaque cone photoreceptors: adaptation, noise, and kinetics. *J. Neurosci.* 19:1203–1216.
- Schuss, Z. 1980. Theory and applications of stochastic differential equations. John Wiley and Sons. New York.
- Steinberg, R. H., S. K. Fisher, and D. H. Anderson. 1980. Disk morphogenesis in vertebrate photoreceptors. *J. Comp. Neurol.* 190:501–508.
- Wissinger, B., F. Muller, I. Weyand, S. Schuffenhauer, S. Thanos, U. B. Kaupp, and E. Zrenner. 1997. Cloning, chromosomal localization and functional expression of the gene encoding the alpha-subunit of the cGMP-gated channel in human cone photoreceptors. *Eur. J. Neurosci.* 9:2512–2521.